

# Lawrence Berkeley National Laboratory

## LBL Publications

### Title

The effect of CO<sub>2</sub>-induced dissolution on flow properties in Indiana Limestone: An in situ synchrotron X-ray micro-tomography study

### Permalink

<https://escholarship.org/uc/item/8z65g7ch>

### Authors

Voltolini, Marco  
Ajo-Franklin, Jonathan

### Publication Date

2019-03-01

### DOI

10.1016/j.ijggc.2018.12.013

Peer reviewed

# The Effect of CO<sub>2</sub>-Induced Dissolution on Flow Properties in Indiana Limestone: an *In Situ* Synchrotron X-Ray Micro-Tomography Study

5

Marco Voltolini<sup>1</sup> and Jonathan Ajo-Franklin<sup>1</sup>

<sup>1</sup> Lawrence Berkeley National Laboratory

## 10 **Abstract**

The injection of CO<sub>2</sub>-rich fluids in carbonate rocks results in an evolution of the pore space, with consequent changes in the hydraulic properties of the reservoir; how these properties evolve, particularly for parameters relevant to multiphase flow e.g.  $P_c(s)$ , remains a topic of active research despite several decades of study. We have carried out an *in situ* synchrotron X-ray microtomography experiment to monitor pore structure evolution during dissolution of an Indiana Limestone core; the experiment involved flowing CO<sub>2</sub>-saturated water through the core for 36 hours and resulted in 10 volumes corresponding to different temporal stages of the dissolution process. The injection parameters corresponded to the flow velocities expected near the well-bore region of a shallow aqueous CO<sub>2</sub> injection; fast flow rates with high reactant availability. Analysis of the tomographic data shows flow-enhanced dissolution i.e. channeling, and provides a time-resolved map of pore space alteration. Using the resulting 4D pore space volume, we modeled the evolution of capillary-pressure curves; this exercise demonstrates how pore structure evolution could impact the invasion and remobilization of non-wetting fluids, dramatically decreasing the entry pressure and the  $P_c$  in some parts of the sample. The modeling of permeability, using a Stokes solver approach, quantified the relationship of porosity vs. permeability; we found that a modest increase in porosity, especially when the channeling system is more developed, greatly affects permeability. These results demonstrate how movement of CO<sub>2</sub> saturated brine near injected plumes might alter drainage dynamics near the plume boundary, thus leading to mobilization across subtle capillary barriers.

35

Keywords: *Limestone dissolution; In-situ synchrotron X-ray microtomography; Porosity evolution; Capillary pressure modeling; Permeability modeling.*

## 40 **1. Introduction**

Geological carbon sequestration (GCS) is current strategy under development for greenhouse gas emission mitigation at an industrial scale. Different approaches for GCS are currently being studied, with a variety of targets for reservoir rocks, typically deep aquifers and depleted oil and gas fields (e.g. Benson and Cole, 2008). In situations where CO<sub>2</sub> value is required for injection and appropriate fields exist near sources, CO<sub>2</sub> enhanced oil recovery (EOR) is an attractive transition strategy. Besides the more “typical” reservoir rocks, usually chosen because their injectivity, proximity, and suitable stratigraphic settings, some rocks with advantageous qualities such as high reactivity, typically volcanic or volcanoclastic reservoir rocks, are also targeted in specific regions (e.g. Mc Grail et al., 2006; Gislason and Oelkers, 2014; general for basalts. Zhang et al., 2015; for volcanogenic sandstones).

GCS relies on four main primary trapping mechanisms: i) structural trapping, where a sealing formation stops the migration of CO<sub>2</sub>, acting as a barrier. ii) capillary trapping, where the CO<sub>2</sub> is trapped by capillary forces in the fluids after the imbibition following the CO<sub>2</sub> injection; iii) solubility trapping, where CO<sub>2</sub> is dissolved in the brine of the reservoir; iv) mineral trapping, where the CO<sub>2</sub> reacts with minerals in the reservoir to precipitate as carbonates (Benson et al., 2005). These mechanisms can be present, and interact, at different times and space in the targeted reservoir and depends on a wide variety of factors, including rock mineralogy, microstructure, and hydraulic properties. Beyond primary structural seals on a GCS reservoir, numerous more subtle low/intermediate permeability features often exist, referred to as “baffles” in clastic systems, which can control larger scale scCO<sub>2</sub> distribution and timescales for mixing and dissolution e.g. examples include thin shales (e.g. Cavanagh and Haszeldine, 2014) and marls in carbonate sequences.

A significant fraction of the targeted storage formations, particularly in an EOR context, are carbonates, or at least carbonates-rich rocks with examples including the Weyburn field (White, 2013) and EOR in the Permian Basin. Carbonates (typically calcite and/or dolomite) readily react with the acidified brine (Peng et al., 2015, for calcite; Baritantonaki et al., 2017, for dolomite). The reactions induced by the acidified fluids can modify the microstructure of the reservoir rock, altering its hydraulic, geochemical, and geomechanical properties (e.g. Mohamed and Nasr-El-Din, 2012), as well as damage the injection wells (e.g. Carroll et al., 2017) and immediate surroundings.

How a reservoir carbonate rock will evolve in a GCS scenario depends on the combination of a wide range of factors, all tightly coupled. Pressure, temperature, and salinity control the maximum amount of CO<sub>2</sub> that can be dissolved in the brine. The mineralogy of the reservoir rock controls its reactivity (e.g. calcite dissolves faster than dolomite, as shown in Deng et al., 2016). The microstructure of the rock (pore-size distribution, crystallinity of the mineral phases, etc.) also has a significant impact on the reactivity of the rock and its evolution (Deng et al., 2016, 2017). The hydraulic properties can exert control on the evolution of the microstructure, e.g. leading towards wormholing, channeling, or more homogeneous dissolution patterns (Ott and Oedai, 2015). Last, the mechanical properties of a rock can be weakened by the dissolution, and cause localized compaction (Grgic, 2011).

90 Given the complexity of this tightly interconnected system, the  
modeling of the phenomena, from pore to basin scales, which is needed to  
predict the evolution of the system during and after the injection, becomes  
extremely challenging. The first step needed is to identify and quantify the  
95 relevant phenomena at the pore scale, including the time evolution of  
porosity, permeability, and multi-phase parameters (e.g. relative permeability  
and  $P_c$  (s)). In this context, a technique such as in-situ X-ray micro computed  
tomography (XR- $\mu$ CT) can provide the information required. XR- $\mu$ CT, when  
properly utilized, has the capacity to observe the evolution of rock  
100 microstructure in 3D while reactions occur. In contrast, many traditional  
petrographic techniques are inherently 2D and destructive. The 3D nature of  
tomographic data can also be used for the characterization of the pore space  
in a quantitative fashion (e.g. Ji et al., 2012, for Indiana limestone), or to  
calculate hydraulic properties in a context of digital rock physics (Knackstedt  
et al., 2009; Andr a et al., 2013). The ability of this technique to provide key  
105 parameters in hydrogeochemical processes is highlighted by the substantial  
number of recent studies targeting the topic of CO<sub>2</sub>-induced dissolution in  
carbonate rocks of interest for GCS, either in the context of reservoir or  
caprock performance (Gouze and Luquot 2011; Menke et al., 2015, 2016; Ott  
and Oedai, 2015; Deng et al., 2016, 2017).

110 Our study aims to understand the dissolution patterns in a generic  
carbonate reservoir rock with a microstructure and mineralogy compatible  
with GCS/EOR targeted reservoir rocks. This experiment is compatible with  
the scenario of a near-wellbore region, where the availability of reactant is  
high and the flow is fast. This is the situation where the evolution is expected  
115 to be the fastest and the most pervasive, and where analogous  
microstructural changes, when occurring in deep reservoirs, translate in  
changes in permeability and entry pressure that might play a key role in the  
distribution of the CO<sub>2</sub> during the injection process. We explore how such a  
system might evolve from a microstructural perspective, its implications on  
120 the hydraulic properties of the rock, and how these can potentially impact the  
injection of CO<sub>2</sub>.

## 2. Materials and Methods

### 125 **2.1. Sample characterization and preparation**

For our in-situ synchrotron X-ray micro-computed tomography (SXR- $\mu$ CT)  
study, a mini core of the Indiana Limestone (from a quarry in the Bedford  
area) was selected (*Kocurek Industries*). The Indiana Limestone is part of the  
Salem Formation (Mississippian) and is currently actively quarried (Indiana  
130 Limestone handbook, 2007) and is actively utilized in core-flood and rock  
physics studies. The sample displays the microstructure of an organogenic  
limestone, with a complex history of recrystallization of the carbonates and  
silica from the original deposition. The textures typical of organogenic CaCO<sub>3</sub>  
are clearly present (fragments of foraminifera, bryozoa, etc.) giving the rock  
135 a typical appearance and a very complex porosity structure at different  
scales. X-ray powder diffraction highlights that the sample is composed  
almost entirely of calcite, with trace amounts of quartz and clays (both <1%  
by weight, as per Rietveld analysis).

140 The complexity of the microstructure of the Indiana Limestone at  
different scales is exemplified in Fig. 1, where SEM images at different  
resolutions are shown. At the millimeter scale (Fig. 1a) the backscattering  
image of a cut section highlights the main microstructure of the rock: the  
main components are oolitic structures (often with a bioclast as the nucleus)  
cemented together, with an interstitial pore space. When progressively  
145 increasing the magnification, as shown in the sequence of secondary  
electrons images in Fig. 1b,c,d, a new hierarchy of structures is visible. The  
ooliths retain most of their original shape, and display the characteristic  
concentric accretion layered structure. When looking at the single layers, it  
is possible to observe that the layers are composed of calcite microcrystals. In  
150 some layers, these crystals are below one micron in size (detail of a detached  
single layer in Fig. 1c). Few isolated perfectly euhedral quartz crystals are  
present as well, as an accessory phase, highlighting the complex  
recrystallization history of the rock. This microstructure is expected to have a  
direct impact on the porosity of the system (as emphasized by Freire-  
155 Gormaly et al, 2015), and at the scale considered we can identify two main  
different porosity segments: i) the interstitial porosity (which is above the  
resolution of the SXR- $\mu$ CT measurement) generated by the aggregation  
structure of the ooliths, and ii) the micro-/nano- porosity generated by the  
space among the single micro-/nano- calcite crystals, which is below the  
160 resolution of the SXR- $\mu$ CT measurement. This porosity distribution has  
potentially a significant impact in the estimate of all the chemical processes  
depending on the reactive surface area values.

The dimensions of the sample used for the in situ SXR- $\mu$ CT experiment  
was a cylindrical core, 8.6 mm in diameter  $\times$  7.7 mm in height, fully imaged  
165 during the experiment; the full volume image enabled recovery of  
appropriate boundary conditions for subsequent flow modeling.

## **2.2. SXR- $\mu$ CT measurement and first data processing**

170 The Indiana Limestone mini-core was placed between two threadless 3/8"  
stainless steel fittings with 1/8" tubing male inlets, and jacketed using  
polyvinylidene fluoride heat-shrink tubing, locked in place on the threadless  
portion of the fittings, and fixed with steel wire. The jacketed sample was  
connected to a high performance liquid chromatography pump set at 0.2  
ml/min constant flow. The sample was first flushed with He, and then  
175 saturated with water to collect the baseline dataset. A stirred reservoir filled  
with water and a headspace of CO<sub>2</sub> kept at ~11 psi (76 kPa) and 28 °C, and  
equilibrated overnight, was used to provide the CO<sub>2</sub> aqueous solution to flow  
through the sample. That pressure was maintained in the flow system via a  
back-pressure regulator.

180 The SXR- $\mu$ CT scans were conducted every 4 hours, providing a total of  
10 datasets covering 36 hours of effective reaction. The SXR- $\mu$ CT  
experiments were carried out at beamline 8.3.2. (MacDowell et al., 2012) at  
the Advanced Light Source (ALS), Lawrence Berkeley National Laboratory  
(LBNL). The beamline setup for this experiment used filter-hardened (2 mm  
185 Al, and 0.5 mm Cu) white light as the radiation source. For this kind of  
experiments the use of white light compared to the monochromatic one is  
advantageous for several reasons, including faster data collection, thus  
minimizing eventual motion artifacts in dynamic experiments, and a larger

vertical field of view. For each time step, a total of three vertical tiles were  
190 collected, to image the entire sample height. During each tomographic data  
collection we acquired 1441 projections over a 180 degrees rotation. The  
exposure time varied from 55 ms to 95 ms, increasing in time to compensate  
for the browning of the objective lens of the detector system, due to  
195 radiation-induced color centers generation in the glass. The detector system  
included a 50  $\mu\text{m}$  Ce:LuAG scintillator, 2 $\times$  objective optics, and a PCO-4000  
CCD camera. The resulting pixel size was 4.4  $\mu\text{m}$ . The sample to detector  
distance was  $\sim$ 5 cm. The tomographic datasets were reconstructed using the  
standard filtered backprojection approach, with a Shepp-Logan filter (Kak and  
200 Slaney, 2001), as implemented in the software Octopus<sup>®</sup> (Dierick et al.,  
2004).

### **2.3. Tomographic Data processing and analysis**

The reconstructed volumes were analyzed using the Fiji software framework  
(Schindelin et al., 2012). The first processing step after reconstruction was  
205 the segmentation of the pore space from the solids. The Otsu thresholding  
algorithm (Otsu, 1979) was used to separate the two classes of objects. The  
volume data 3D visualization was carried out using the VG Studio<sup>®</sup> 2.0  
software. A cylindrical cropping of the volumes, to cut the inlet and outlet  
steel fitting ends and the jacket, was also done to obtain a cylinder with only  
210 the rock sample. Given the precise coring and mounting of the sample, only a  
very small amount ( $\sim$ 100  $\mu\text{m}$ ) of sample was cut during the cropping  
procedure. No evidence of preferential flow along the jacket, or any other  
anomalous behavior, was observed in the extracted imagery. The segmented  
volumes were used for the first pore space analysis, with a slice-by-slice  
215 porosity calculation to highlight the localization of the dissolution, i.e. the  
extent of dissolution in function of the distance from the inlet. The Local  
Thickness (LT) approach (Dougherty and Kunzelmann, 2007) was chosen to  
analyze the evolution of the pore space during the reaction, since it is easy to  
calculate, does not require an artificial distinction between pores and throats,  
220 and provides useful information about which class of features evolve. The  
same LT attribute is the starting point for the digital rock physics model we  
use to calculate drainage behavior.

#### *2.3.1. Modeling the evolution of the capillary pressure curves*

225 Once the pore space local thickness volumes for each time step have been  
calculated, we calculate the capillary pressure curves for a perfectly non-  
wetting fluid following the approach described in Voltolini et al. 2017, where  
we refer the reader for the details; this approach is based on the maximum  
inscribed spheres concept as presented by Silin et al., 2011. The main  
230 advantages of this approach are that it is fast to calculate, it needs only a  
binary volume of the pore space as a starting point, and has already proved  
effective in modeling both the 3D distribution of supercritical CO<sub>2</sub> at reservoir  
conditions, and mercury intrusion pycnometry curves, albeit with a smaller  
range of porosity values, limited by the resolution of the imaging setup. The  
235 approach is purely geometrical in nature which makes it straightforward to  
implement and computationally efficient. The main limitation is that it  
neglects several factors including (i) the contact angle of the invading fluid,  
which is always considered perfectly non-wetting and (ii) dynamic effects

240 present at high capillary numbers. This first limitation is negligible when  
simulating the very first stage of drainage of scCO<sub>2</sub> in markedly water-wet  
systems (as we consider the one presented in this work), or Hg intrusion (as  
demonstrated in Voltolini et al. 2017), but cannot be used on systems with  
partial, evolving, or mixed, wettability.

#### 245 2.3.2. Modeling the evolution of the permeability

With the dissolution of the calcite during the experiments, the evolution of  
the pore space should clearly impact the permeability of the system. Giving  
the challenges of experimental permeability measurements on mm  
dimension samples, we decided to use a modeling approach to retrieve  
250 permeability from the 4D volumes. The permeability in the different datasets  
was calculated using a Stokes flow solver, similar to the one published in Silin  
and Patzek (2009), as presented in Zuo et al., (2017) which utilized the same  
implementation we selected. The permeability calculation has been carried  
out on 250 vx cubic subvolumes of the sample, rescaled at 17.6  $\mu\text{m}$  per vx,  
255 resulting in a cube with a 4.4 mm side, including most of the measured  
sample. This approach is not only helpful to estimate the evolution of the  
permeability, but the generation of the velocity fields also allows better  
visualization of the presence and time evolution of preferential flowpaths.

### 260 3. Results and discussion

The first step in analyzing the results is a qualitative inspection of the volume  
renderings of sequential SXR- $\mu\text{CT}$  reconstructions. In Fig. 2, two full  
sequences of the volume renderings are presented, with each time step  
being 4h, with the top half showing a vertical virtual cut, while the bottom  
265 half shows a horizontal cut about 1 mm from the inlet, viewed from the top  
(inlet). The evolution of the microstructure of the sample is clear, highlighted  
by the increase in porosity with time. This increase in porosity seems clearly  
more pronounced closer to the inlet, as can be seen from the vertical cut  
sequence. From the horizontal section, it is possible to identify which parts of  
270 the sample dissolve preferentially; the small features, such as thin fragments,  
and detached/isolated oolite layers seem to dissolve faster than the more  
“blocky” parts of the sample such as the solid oolites. This is to be expected,  
assuming equal reactant availability conditions, given the different reactive  
surface area available. In addition, some pores display faster dissolution rates  
275 than others, hinting at issues of different reactant supply controlled by  
preferential flowpaths. Both sample microstructure (more reactive surface  
area induces faster dissolution) and hydraulics (faster reactant supply causes  
faster dissolution) involve the local reaction rate of the material and the  
subsequent dynamic modification of the flowpaths.

280 Following these general observations, we can more precisely visualize  
the evolution, highlighting where and when the dissolution process occurred.  
One approach is to build a volume where the dissolved material is color-  
labeled with respect to time, providing a map of sequential dissolution  
surfaces This is carried out by using a XOR operator on each binary volume  
285 (pore space) with the previous one in the dissolution sequence, after volume  
registration, and finally color-label the result of each cycle and build a single  
volume. In Fig. 3 captures the dissolution process using this type of  
visualization: a thin ( $\sim 250 \mu\text{m}$ ) vertical slice of the volume has been virtually

cut, and on the left the volume rendering of the sample at the end of the  
290 experiment has been superimposed with the color-labeled volume  
representing the dissolved material. In the right panel of Fig. 3, only the latter  
volume is shown, for clarity. The use of a thin section of the sample helps to  
better appreciate the local features in such a complex microstructure. From  
this volume more precise information can be obtained. The material dissolved  
295 at the early stages (e.g. the blue color represents the material dissolved in  
the first 4 hours) is often associated with pore-filling calcite with a large  
apparent surface area or thin detached oolite laminae (similar to the one in  
Fig. 1c). This dissolution pattern can be seen in Fig. 3 where the blue-labeled  
regions, representing regions dissolved in the first 4-8 hours, are dominated  
300 by interstitial calcite regions. Often this material displays a slightly darker  
graylevel, i.e. it is less X-ray attenuating. Since the sample consists almost  
entirely of calcite, the darker graylevels are due to partial volume effects  
induced by sub-resolution micro/nanoporosity. Considering the more rapid  
dissolution in these regions, such nanoporosity is likely linked to higher local  
305 reactive surface areas.

As we follow the color code of the look-up table in Fig. 3 approaching  
the end of the reaction, we can see that the dissolution tends to concentrate  
on a specific population of pores (orange-red-white colors); in other pores the  
dissolution stops or proceeds very slowly. This is evidence of the evolution of  
310 the hydraulic properties of the sample generated by the dissolution: as  
dissolution proceeds, the creation of preferential flowpaths tends to  
progressively concentrate the reaction in those specific parts of the sample.  
This phenomena of localized preferential dissolution, referred to as  
wormholing, channeling, etc. have been observed several times in reactive  
315 transport experiments in carbonates (Fredd and Fogler, 1998; Siddiqui et al,  
2006; Menke et al., 2016).

To describe the evolution of the pore space in a more quantitative  
fashion, we evaluated porosity on a slice-by-slice basis to examine dissolution  
trends across the sample. In Fig. 4a the slice-by-slice porosity plots are  
320 shown, following the orientation of the volume rendering figures (inlet at the  
top). A first observation is that during the initial 4 hours, the dissolved  
volume was larger than in the following time increments. This behavior can  
also be observed in Fig. 3 where the blue color is more prevalent than the  
others. Combining the information from the two figures we can develop a  
325 hypothesis: during the first stages of dissolution, strong preferential  
pathways are not developed, hence the dissolution of reactive material is  
more uniform. In addition to that, at the first stage more material with large  
reactive surface areas (isolated/detached oolite lamellae, loose “powdery”  
calcite, etc.), and therefore with faster dissolution rates, is present as well.  
330 With a more homogeneous flow, and the larger availability of reactive  
components, it is not surprising to observe a faster dissolution rate at the first  
stage of the experiment. The second observation from Fig. 4a is that net  
dissolution decreases as function of the distance from the inlet.

Another feature that can be observed from Fig. 4a is the presence of  
335 specific zones with higher dissolution rates. When looking at the porosity  
curves around slice #100, the plot in the unreacted sample is rather flat.  
While the reaction proceeds, particularly during the first 8 hours, it is possible  
to observe the generation of a new peak, meaning higher amounts of



340 dissolved materials and subsequent porosity is localized in that sample  
region. These newly formed peaks highlight portions of the sample where the  
dissolution was faster, and seem to be unrelated to porosity features present  
in the unreacted rock, i.e. they do not depend on the starting porosity value.  
Again, this behavior is likely due mostly to the presence of materials with  
345 textures resulting in high RSA values and the existence of preferential  
flowpaths enhancing local dissolution.

An alternative approach to evaluating pore space evolution is  
examination of local thickness histograms, an unbiased view of pore  
dimension modification. Fig. 4b depicts the time evolution of local thickness;  
as can be seen, the dominant process is an increase in abundance of small to  
350 intermediate size pores/throats in the 10-30 micron range. As the dissolution  
continues, flow localization results in larger dissolution features, shifting the  
newly created porosity to larger thickness/diameter values. The progressive  
nature of this phenomenon (the higher the reaction extent, the larger the size  
of the local thickness fraction that grows) is also observable at the “shoulder”  
355 of the curves, growing more and more towards the large local thickness  
values. This type of analysis suggests that local thickness is an excellent  
geometric proxy for tracking the evolution of channeling in an evolving  
porous system.

The behavior observed in both porosity and LT analysis, with the  
360 generation of preferential flowpaths getting larger with the evolution of the  
system, is a channeling behavior observed in Menke et al., 2017 in a similar  
experiment involving CO<sub>2</sub>-induced dissolution in limestone samples. The  
characteristic evolution of the pore space in such reactive systems can be, in  
theory, inferred by understanding the system in terms of the dimensionless  
365 Damkhöler and Péclet numbers, representing the ratios of advection to  
reaction, and the diffusion to advection times, respectively. The two numbers  
have been calculated following Menke et al. (2017); we adopt the following  
formulas for consistency,

$$370 \quad Da = \frac{\pi r}{U_{av} n} \quad 1)$$

$$Pe = \frac{U_{av} L}{D} \quad 2)$$

where  $r$  is the reaction rate for calcite, as measured at similar P/T conditions  
375 in Plummer et al. (1978) and  $U_{av}$  is the average velocity of the fluid in the  
pore space (as derived from the Stokes flow model). Likewise,  $n$  is defined as  
 $\rho_{cc}(1-\phi)/M_{cc}$ , where  $\rho_{cc}$  is the density of pure calcite,  $\phi$  is the total porosity,  
and  $M_{cc}$  is the molecular mass of calcite. The value of the porosity used here  
is the one obtained via the tomographic dataset, therefore the nanoporosity  
380 present in the sample is not accounted for.  $L$  is the characteristic length  
defined as  $\pi/SA$ , where  $SA$  is the surface area. The  $SA$  has been calculated by  
measuring the total surface of the pore space from the tomographic dataset,  
corrected with the roughness of the surface of an oolite as measured via SEM  
imaging, at higher resolution, to take into account the granular nature of the  
385 surfaces. A roughness correction factor  $R_c = 72.8$  has been applied to the

surface area value calculated from the tomographic dataset to derive the SA. This correction should, at least partially, take into account the features below the SXR- $\mu$ CT resolution that can potentially have a significant effect on the dissolution rates of the material. Based on these assumptions, the values found for the starting sample were:  $Da = 3.9 \cdot 10^{-4}$  and  $Pe = 3.3 \cdot 10^3$ . A low value for  $Da$  suggests a state where the reaction rate is slow compared to the advection, and a high  $Pe$  indicates that advection dominates compared to diffusion, a condition compatible with the development of channels observed in the experiment. These values seem to agree also with the values found in Menke et al. (2016), given the different experimental conditions (and samples) and the different methods used to estimate  $\phi$  and SA.

### **3.1. Evolution of capillary pressure distribution: effects on drainage**

The localized dissolution of the sample during flow and reaction, as described in the previous section, is expected to modify hydraulic properties. The first topic addressed in this context is the evolution of the drainage properties of the rock. When considering GCS and/or EOR scenarios, such an evolution of the pore space can have a significant impact on the entry pressure of a non-wetting fluid (such as supercritical  $\text{CO}_2$  or oil). This variation in entry pressure could modify the  $\text{scCO}_2$  migration pathways in a reservoir by enabling plume expansion into regions initially. The measurement of capillary pressure ( $P_c$ ) curves is commonly estimated using Hg intrusion pycnometry. Hg pycnometry is a destructive test and hence cannot be used to monitor evolution of a pore system during reaction. As we presented in Voltolini et al. (2017) and had been earlier proposed in Silin et al. (2011), we have developed a code enabling calculation of  $P_c$  curves using tomographic datasets only; consequently, the approach can be applied to a sequence of volumes from dissolution experiments to probe alteration of parameters such as entry pressure. It is worth emphasizing that this digital rock physics approach, even with intrinsic limitations such as resolution and field of view constraints, enables virtual measurements that could not be executed experimentally.

We imposed the top of the sample as the inlet boundary (as in the real experiment); for each dataset, we calculated the invaded volumes as a function of the decrease in throat size, corresponding to an increase of the  $P_c$ . This process resulted in the generation of 970 volumes with the calculated invading fluid distribution, at any given reaction time and throat size, available. The calculation of the volumes required 24h on a desktop PC. In Fig. 5, the calculated invading fluid is displayed in yellow. On the left, the calculated radiographs of the invading fluid for three porosity states during dissolution and three steps of increasing  $P_c$ ; this provides an example of the difference in the distribution of a non-wetting phase expected at for different alterations of the pore space. On the right, the actual calculated 3D volume rendering of the modeled radiograph in the center is shown, superimposed over the (vertically cut) measured volume of the sample, to provide context.

With this rich dataset spanning both dissolution state and invasion, it is possible to obtain a  $P_c$  surface, since we can add the extra dimension of reaction time during dissolution. This surface is plotted in Fig. 6, where for each "step" in the  $P_c$  surface, a calculated volume of the invading fluid has

been calculated. Three of these volumes are shown, taken from the  $P_c$  curve of the volume after 20 hours of reaction, for different throat sizes. From the  $P_c$  surface it is possible to appreciate how the entry pressure varies significantly with the extent of the reaction. This is due to a combination of both the increase in porosity in general, but especially to the increase in the largest pore/throat, and more specifically the local thickness values close to the inlet. From the surface plot it is also possible to obtain  $P_c$  sections along the reaction extent. If we assume an experimental condition comparable with the experiment and relative drainage model presented in Voltolini et al., 2017, we can follow the evolution of  $P_c$  for a throat size value of 105.6  $\mu\text{m}$  (the value found able to simulate the experimental drainage data): in the unreacted sample, the invaded volume would be extremely small, around 1%, while the sample would become more and more prone to be invaded with the evolution of the pore space, ending with an invaded volume (total volume of the sample) by  $\text{scCO}_2$  of 8.8% i.e. a large fraction of the pore space connected to the inlet. The increase in throat size close to the inlet makes the first step of invasion much easier, and the dissolution along the preferential flowpaths creates large channels where the  $P_c$  is low. These pathways provide easy primary access (connectivity) to the other pores with smaller local thickness values, so when the  $P_c$  is increased they are progressively invaded.

The channeling effect is also visible from the  $P_c$  surface; when looking at the single  $P_c$  profiles an evolution of the shape of the single profiles is clear. For the less reacted samples the increase is progressive, with the sudden increase in the invaded volume for small throat size values, meaning that the bulk of the pore space is dominated by small throats, and when the  $P_c$  is high enough to overcome the bottlenecks the volume is quickly invaded. The reacted volume exhibits different characteristics; the evolution of channeling systems provides the invading fluid an easy accessible pathway, marked by the growth of a shoulder on the  $P_c$  profile. The shoulder appears when the enlarged channels are invaded, early in the process, and subsequently the porosity connected to the main flowpaths by the smaller throats is invaded, generating the increase in invaded volume in the higher  $P_c$  part of the curve. These results obtained with the modeling of the drainage process complement the morphologic observations of the tomographic datasets.

### **3.2. Permeability evolution**

Another opportunity provided by the digital rock physics approach is the calculation of the evolution of the single phase permeability of the system during the reaction. Direct permeability measurements on small (mm) samples in complex experimental cells are challenging due to the subtle pressure drop induced by permeable samples and the large effect of tubing runs; in these situations, direct numerical modeling using tomographic data becomes attractive. The method used for this model is based on the direct simulation of Stokes flow, using the model developed by Zuo et al., 2017 (Explained in detail in Appendix A). The goal in this case is to numerically determine the porosity/permeability relationship for this particular dissolution path. In Table 1, both relative and absolute values of permeability and porosity (baseline, the starting unreacted sample = 1) are summarized, with permeability values calculated via the Stokes solver, and porosity values

calculated from the analysis of the tomographic datasets. From these values, we can observe that the value of porosity has close to doubled at the end of the experiment, increasing from 11% to 21%. As is clear from the prior sections however, this change is likely an oversimplification of the system given the heterogeneity of the dissolution process and presence of sub-resolution porosity in the baseline volume.

If we consider the permeability values, we can observe that the permeability at the end of the experiment is 23 times the value of the baseline sample. In Fig. 7 (top) the plots of permeability and porosity are shown. From these curves we can see how the porosity increases significantly in the first stages of the reaction. From the graph, a temporary decrease in the reaction can be seen, visible between  $t = 16$  h and 20 h. The reason for this specific behavior is unclear, and no noticeable issues during the experiment were detected. The permeability values almost constantly increase in the first half of the experiment, followed by a more rapid, exponential growth, at late times as the channeling system further develops. At the bottom of the Fig. 7, three volumes, corresponding to the labels a), b), and c) in the graph above, are shown for different reaction times, with the velocity fields of the fluid displayed in color. At  $t = 20$  h the presence of some channeling features, with faster flow velocities, starts to appear, especially around the inlet zone. At  $t = 36$  h the presence of a channeling system is clear, particularly in the zones closer to the inlet (top). A relevant question is the quantitative relationship between porosity and permeability in this system. Plotting the porosity vs. permeability curve (Fig. 8), we can see a clear pattern. The fit of those values with a power law function is almost perfect.

$$k \propto \phi^\alpha \quad 3)$$

From the equation of the function (3) we can find the exponent  $\alpha$  close to 5. This is a value very similar to the one found for a sample with a similar behavior in Menke et al. (2017), and different than the value of 3 used in the Kozeny-Carman relation, as found also in other systems (e.g. Fontainebleau sandstone, in Bourby et al., 1987). This latter example is one of those where the exponent value varies with the porosity, meaning that the fit of the data along the whole porosity interval with a power law function, with a constant  $\alpha$ , is not correct. These observations suggest that a sub-scale porosity/permeability relationship might be useful for larger reactive transport models, where the functional form  $\alpha$  is dependent on local estimates of Damkhöler and Péclet numbers, thus capturing the non-uniformity of such relationships across different pore-structure evolution paths.

In our sample the value of 5 is constant for all the intervals (no outliers) in the considered porosity interval, as also highlighted by the high quality fit ( $R^2 \approx 1$ ) of the measured data with the plotted function. The values of  $\alpha$  for evolving systems have been measured, with a focus on the diagenetic processes (e.g. Bernabé et al., 2003) and it has been found to be rather variable, depending on the sample and processes observed. An experiment involving the dissolution of a compact limestone (McCune et al., 1979) instead found very large values for  $\alpha$  ( $>20$ ). A larger value ( $\alpha = 13$ )

was found from a more homogeneously dissolving limestone, measured via dynamic in situ SXR- $\mu$ CT as presented in Noriel et al. (2005).

#### 4. Conclusions

540 This work presents observations of pore-structure evolution of a limestone during dissolution induced by a CO<sub>2</sub>-rich fluid, followed by a modeling study to quantify likely impacts on hydraulic properties. This topic is of relevance to both GCS and EOR operations, where the variations in the hydraulic properties of the reservoir rock due to geochemical reactions can potentially  
545 have a significant impact on flow distribution in the field. We have studied the phenomena at the pore scale using in-situ SXR- $\mu$ CT, monitoring the evolution of the microstructure of the sample with time, while flowing the reactant, and using the datasets obtained to characterize the kind of pore space evolution, and then model the hydraulic properties of the sample. We have found that  
550 the system evolves, developing a channeling dissolution pattern. With time, the dissolution becomes more pronounced along preferential flowpaths. At the beginning of the experiment, the dissolution is more homogeneous and diffuse, when preferential flowpaths are not established and highly reactive material is available. With the increase in extent of the reaction, preferential  
555 flowpaths develop and positive feedbacks with dissolution enlarge these features, particularly close to the inlet where the amount of available reactant is higher.

Such an evolution of the morphology of the pore space significant impacts the hydraulic properties of the sample. The modeled  $P_c$  curves as a  
560 function of reaction extent show a dramatic decrease in entry pressure, coupled with a large increase in invaded volume for a given throat size, as dissolution proceeds. The decrease in entry pressure is explained by the enhanced dissolution close to the inlet; the increase in invaded volume with the reaction at constant throat size (or the equivalent  $P_c$ ) is easily explained  
565 by the development of the large channels along the preferential flowpaths still well connected to the inlet. This channeling effect also has a significant impact on the single-phase permeability of the system. We have calculated the permeability using a Stokes solver and studied its relationship with porosity. While the porosity almost doubles, the increase in permeability of  
570 the system at the end of the experiment is 23 times the starting value. A power law fit of the porosity vs. permeability highlights how the increase in permeability is larger than the value predicted by the classic Kozeny-Carman equation, but is consistent with similar experiments in literature (Menke et al., 2017).

575 We should note that the experiment presented here does not accurately represent the conditions of typical GCS or EOR reservoirs. We focus on the evolution of pore space due to chemical dissolution and its potential impact in different scenarios via a digital rock physics approach. The high flow rates and the high availability of the reactant makes this  
580 scenario more similar to a shallow near well bore region, during the injection of CO<sub>2</sub>. The large increase in permeability due to this channeling effect could increase injectivity. An important zone to consider would be regions near the well bore which are initially not invaded due to lower permeability; these features could be sensitive to dissolution, particularly if secondary brine  
585 transport due to density driven flow were significant. Another relevant

component of the system would be near a seal failure where carbonated brine could be driven by overpressure. In terms of non-wetting fluid mobilization, the generation of channels creates flowpaths where the  $P_c$  is significantly decreased, creating preferential pathways where the remobilized non-wetting fluid can move easily.

We have shown the new opportunities opened by coupling in-situ XR- $\mu$ CT coupled with digital rock physics models. This combination of technologies allows the simulation of difficult or impossible experiments on evolving systems, in this case enabling the quantification of multiphase hydraulic properties during aqueous phase dissolution of a carbonate sample.

### **Acknowledgements**

This work was supported as part of the Center for Nanoscale Control of Geologic CO<sub>2</sub> (NCGC), an Energy Frontier Research Center funded by the U.S. Department of Energy, Office of Science, Basic Energy Sciences under Award # DE-AC02-05CH11231. The SXR- $\mu$ CT experiment was performed with the assistance of Alastair MacDowell and Dula Parkinson at the Advanced Light Source, Beamline 8.3.2, supported by the U.S. DOE Office of Science, Office of Basic Energy Sciences (DE-AC02-05CH11231). Dr. Lin Zuo and Prof. Sally Benson are acknowledged for sharing the Stokes solver code developed at LBNL and Stanford University.

## 610 **References**

- Andrä, H., Combaret, N., Dvorkin, J., Glatt, E., Han, J., Kabel, M., Keehm, Y., Krzikalla, F., Lee, M., Madonna, C. and Marsh, M., 2013. Digital rock physics benchmarks—Part II: Computing effective properties. *Computers & Geosciences*, 50, pp.33-43.
- 615 Baritantonaki, A., Bolourinejad, P. and Herber, R., 2017. An experimental study of dolomite dissolution kinetics at conditions relevant to CO<sub>2</sub> geological storage. *Petroleum Geoscience*, 23(3), pp.353-362.
- 620 Benson, S., Cook, P., Anderson, J., Bachu, S., Nimir, H.B., Basu, B., Bradshaw, J., Deguchi, G., Gale, J., von Goerne, G. and Heidug, W., 2005. Underground geological storage. *IPCC special report on carbon dioxide capture and storage*, pp.195-276.
- 625 Benson, S.M. and Cole, D.R., 2008. CO<sub>2</sub> sequestration in deep sedimentary formations. *Elements*, 4(5), pp.325-331.
- Bernabé, Y., Mok, U. and Evans, B., 2003. Permeability-porosity relationships in rocks subjected to various evolution processes. *Pure and Applied Geophysics*, 160(5), pp.937-960.
- 630 Bourbie, T.O. Coussy, B. Zinszner. 1987. Acoustics of Porous Media. *Gulf Publishing Co, Houston, Texas*.
- 635 Carroll, S.A., Iyer, J. and Walsh, S.D., 2017. Influence of Chemical, Mechanical, and Transport Processes on Wellbore Leakage from Geologic CO<sub>2</sub> Storage Reservoirs. *Accounts of Chemical Research*.
- 640 Cavanagh, A.J. and Haszeldiner, R.S., 2014. The Sleipner storage site: Capillary flow modeling of a latered CO<sub>2</sub> plume requires fractured shale barriers within the Utsira formation. *International Journal of Greenhouse Gas Control*, 21, pp. 101-112.
- 645 Deng, H., Molins, S., Steefel, C., DePaolo, D., Voltolini, M., Yang, L. and Ajo-Franklin, J., 2016. A 2.5 D reactive transport model for fracture alteration simulation. *Environmental science & technology*, 50(14), pp.7564-7571.
- Deng, H., Voltolini, M., Molins, S., Steefel, C.I., DePaolo, D.J., Ajo-Franklin, J. and Yang, L., 2017. Alteration and erosion of rock matrix bordering a carbonate-rich shale fracture. *Environmental Science & Technology*.
- 650 Dierick, M., Masschaele, B. and Van Hoorebeke, L., 2004. Octopus, a fast and user-friendly tomographic reconstruction package developed in LabView®. *Measurement Science and Technology*, 15(7), p.1366.
- 655 Dougherty, R. and Kunzelmann, K.H., 2007. Computing local thickness of 3D structures with ImageJ. *Microscopy and Microanalysis*, 13(S02), p.1678.
- Fredd, C.N. and Fogler, H.S., 1998. Influence of transport and reaction on wormhole formation in porous media. *AIChE journal*, 44(9), pp.1933-1949.
- 660 Gislason, S.R. and Oelkers, E.H., 2014. Carbon storage in basalt. *Science*, 344(6182), pp.373-374.

- 665 Gouze, P. and Luquot, L., 2011. X-ray microtomography characterization of porosity, permeability and reactive surface changes during dissolution. *Journal of contaminant hydrology*, 120, pp.45-55.
- Grgic, D., 2011. Influence of CO<sub>2</sub> on the long-term chemomechanical behavior of an oolitic limestone. *Journal of Geophysical Research: Solid Earth*, 116(B7).
- 670 Freire-Gormaly, M., Ellis, J.S., Bazylak, A. and MacLean, H.L., 2015. Comparing thresholding techniques for quantifying the dual porosity of Indiana Limestone and Pink Dolomite. *Microporous and Mesoporous Materials*, 207, pp.84-89.
- 675 Indiana Limestone Handbook; Indiana Limestone Institute of America, 22nd edition, 2007.
- Ji, Y., Baud, P., Vajdova, V. and Wong, T.F., 2012. Characterization of pore geometry of Indiana limestone in relation to mechanical compaction. *Oil & Gas Science and Technology-Revue d'IFP Energies nouvelles*, 67(5), pp.753-775.
- 680 Kak, A.C. and Slaney, M., 2001. *Principles of computerized tomographic imaging*. Society for Industrial and Applied Mathematics.
- 685 Knackstedt, M.A., Latham, S., Madadi, M., Sheppard, A., Varslot, T. and Arns, C., 2009. Digital rock physics: 3D imaging of core material and correlations to acoustic and flow properties. *The Leading Edge*, 28(1), pp.28-33.
- 690 MacDowell, A.A., Parkinson, D.Y., Haboub, A., Schaible, E., Nasiatka, J.R., Yee, C.A., Jameson, J.R., Ajo-Franklin, J.B., Brodersen, C.R. and McElrone, A.J., 2012, October. X-ray micro-tomography at the Advanced Light Source. In *Proc. SPIE* (Vol. 8506, p. 850618).
- 695 McGrail, B.P., Schaef, H.T., Ho, A.M., Chien, Y.J., Dooley, J.J. and Davidson, C.L., 2006. Potential for carbon dioxide sequestration in flood basalts. *Journal of Geophysical Research: Solid Earth*, 111(B12).
- 700 Menke, H.P., Bijeljic, B., Andrew, M.G. and Blunt, M.J., 2015. Dynamic three-dimensional pore-scale imaging of reaction in a carbonate at reservoir conditions. *Environmental science & technology*, 49(7), pp.4407-4414.
- 705 Menke, H.P., Andrew, M.G., Blunt, M.J. and Bijeljic, B., 2016. Reservoir condition imaging of reactive transport in heterogeneous carbonates using fast synchrotron tomography—Effect of initial pore structure and flow conditions. *Chemical Geology*, 428, pp.15-26.
- 710 Mohamed, I.M. and Nasr-El-Din, H.A., 2012, January. Formation damage due to CO<sub>2</sub> sequestration in deep saline carbonate aquifers. In *SPE International Symposium and Exhibition on Formation Damage Control*. Society of Petroleum Engineers.
- 715 Noiriel, C., Bernard, D., Gouze, P. and Thibault, X., 2005. Hydraulic properties and microgeometry evolution accompanying limestone dissolution by acidic water. *Oil & gas science and technology*, 60(1), pp.177-192.
- Oldenburg, C.M., Stevens, S.H. and Benson, S.M., 2004. Economic feasibility of carbon sequestration with enhanced gas recovery (CSEGR). *Energy*, 29(9), pp.1413-1422.



- Otsu, N., 1979. A threshold selection method from gray-level histograms. *IEEE transactions on systems, man, and cybernetics*, 9(1), pp.62-66.
- 720 Ott, H. and Oedai, S., 2015. Wormhole formation and compact dissolution in single- and two-phase CO<sub>2</sub>-brine injections. *Geophysical Research Letters*, 42(7), pp.2270-2276.
- 725 Peng, C., Crawshaw, J.P., Maitland, G.C. and Trusler, J.M., 2015. Kinetics of calcite dissolution in CO<sub>2</sub>-saturated water at temperatures between (323 and 373) K and pressures up to 13.8 MPa. *Chemical Geology*, 403, pp.74-85.
- 730 Schindelin, J., Arganda-Carreras, I., Frise, E., Kaynig, V., Longair, M., Pietzsch, T., Preibisch, S., Rueden, C., Saalfeld, S., Schmid, B. and Tinevez, J.Y., 2012. Fiji: an open-source platform for biological-image analysis. *Nature methods*, 9(7), pp.676-682.
- 735 Siddiqui, S., Nasr-El-Din, H.A. and Khamees, A.A., 2006. Wormhole initiation and propagation of emulsified acid in carbonate cores using computerized tomography. *Journal of Petroleum Science and Engineering*, 54(3), pp.93-111.
- 740 Silin, D.B. and Patzek, T.W., 2009, January. Predicting relative-permeability curves directly from rock images. In *SPE Annual Technical Conference and Exhibition*. Society of Petroleum Engineers.
- 745 Silin, D., Tomutsa, L., Benson, S.M. and Patzek, T.W., 2011. Microtomography and pore-scale modeling of two-phase fluid distribution. *Transport in porous media*, 86(2), pp.495-515.
- 750 Voltolini, M., Kwon, T.H. and Ajo-Franklin, J., 2017. Visualization and prediction of supercritical CO<sub>2</sub> distribution in sandstones during drainage: An in situ synchrotron X-ray micro-computed tomography study. *International Journal of Greenhouse Gas Control*, 66, pp.230-245.
- 755 White, D., 2013. Seismic characterization and time-lapse imaging during seven years of CO<sub>2</sub> flood in the Weyburn field, Saskatchewan, Canada. *International Journal of Greenhouse Gas Control*. 16S. pp. S78-S94.
- 760 Zhang, S., DePaolo, D.J., Voltolini, M. and Kneafsey, T., 2015. CO<sub>2</sub> mineralization in volcanogenic sandstones: geochemical characterization of the Etchegoin formation, San Joaquin Basin. *Greenhouse Gases: Science and Technology*, 5(5), pp.622-644.
- 765 Zuo, L., Ajo-Franklin, J.B., Voltolini, M., Geller, J.T. and Benson, S.M., 2017. Pore-scale multiphase flow modeling and imaging of CO<sub>2</sub> exsolution in Sandstone. *Journal of Petroleum Science and Engineering*, 155, pp.63-77.

770



## Figure captions

775

Fig. 1

SEM analysis of the sample. a) Back-scattering electrons imaging of a polished section of the sample. b, c, e) Secondary electrons (SE) imaging of the microstructure of the sample at increasing magnification.

780

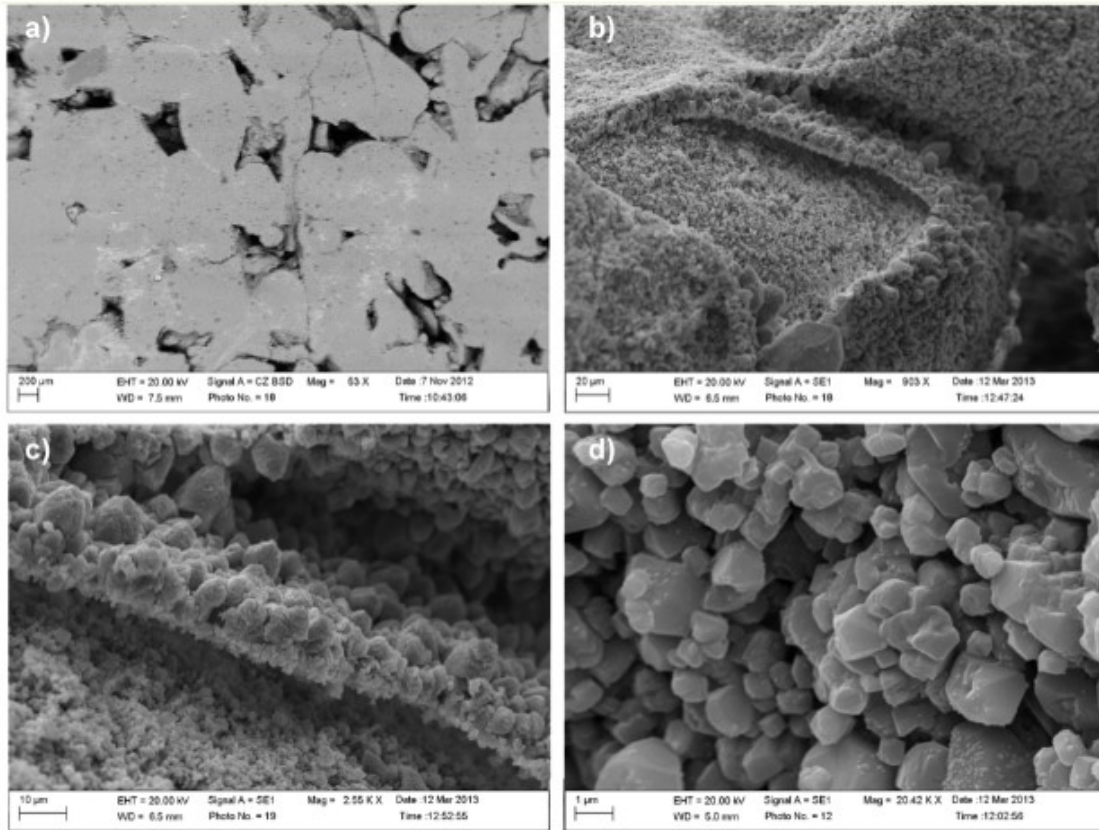
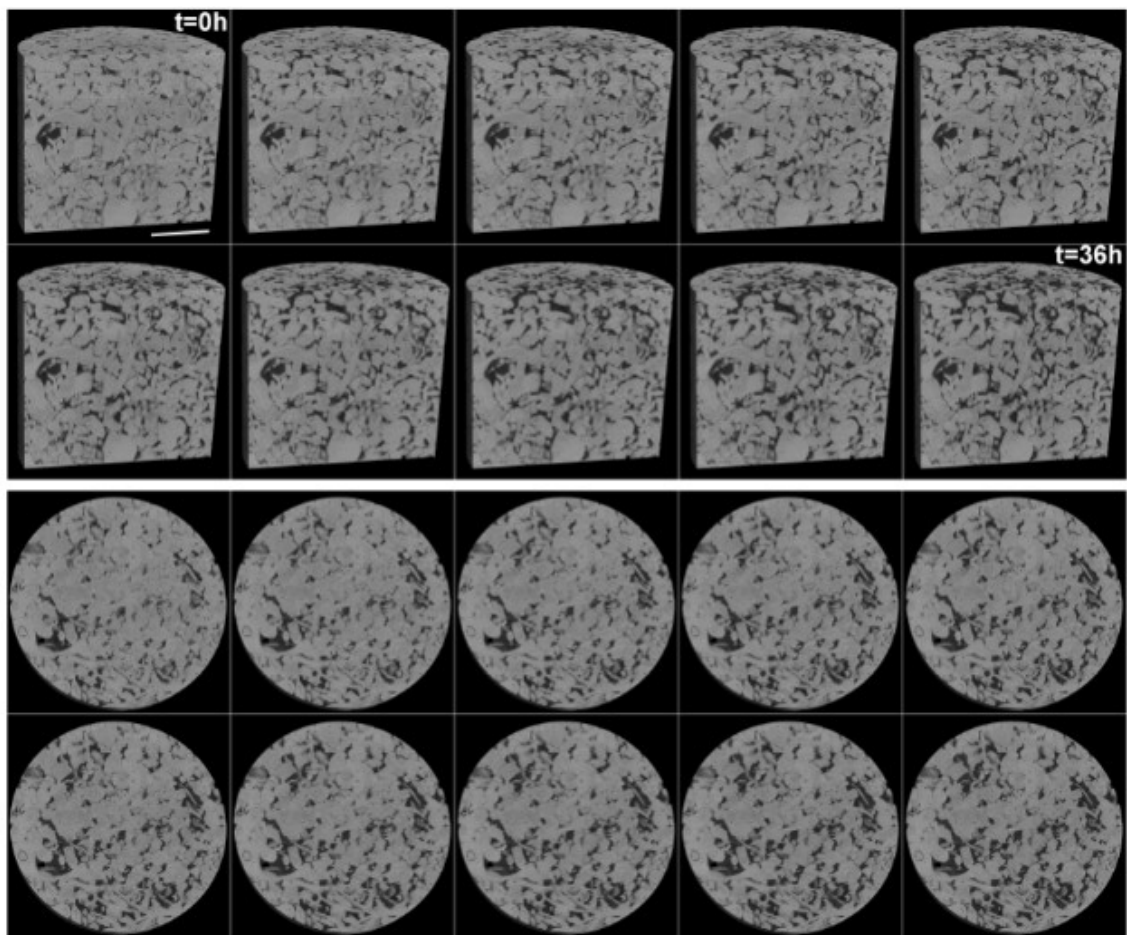


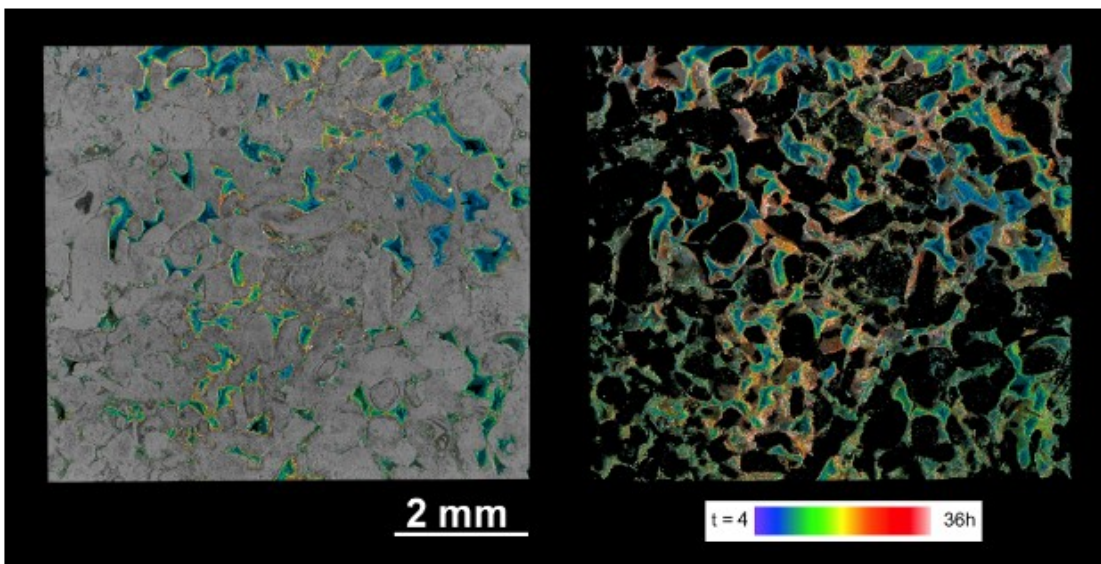
Fig. 2

785 Volume renderings showing the sequence of the 10 time steps of the experiment, where the sample was measured every 4 hours. The upper half shows a vertical virtual cut (inlet at the top), while the lower half shows a horizontal section about 1 mm under the inlet.



790

Fig. 3  
Volume rendering of a vertical thin slab of the sample. The color labeling show the dissolved parts of the sample at the different time steps.



795

Fig. 4

a) Slice-by-slice porosity evolution of the sample. b) Evolution of the local thickness values of the pore space.

800

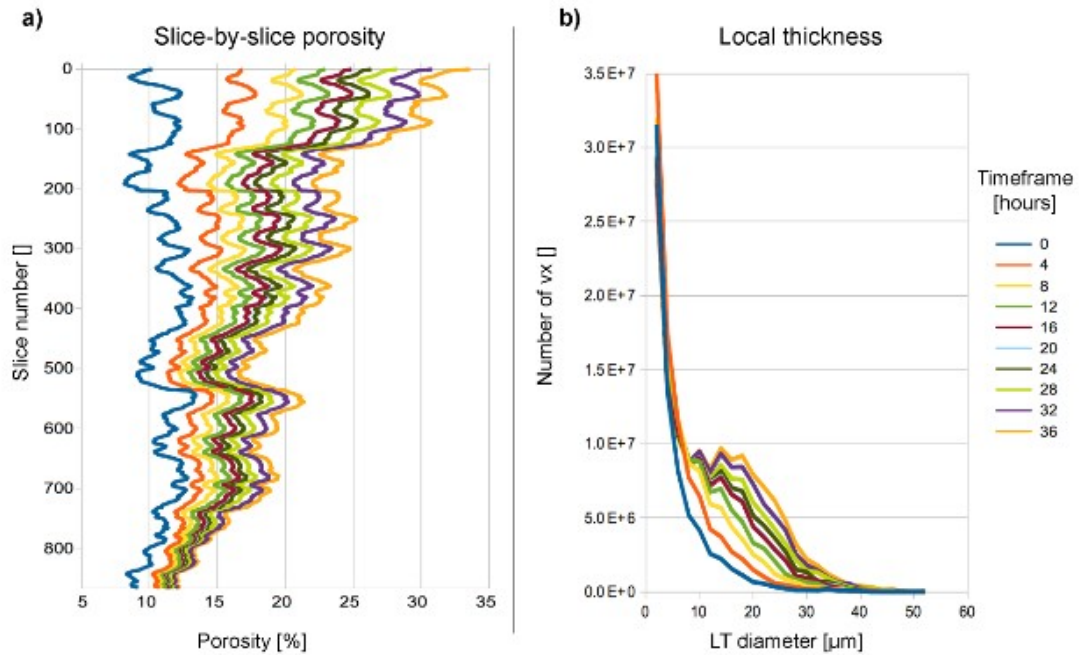
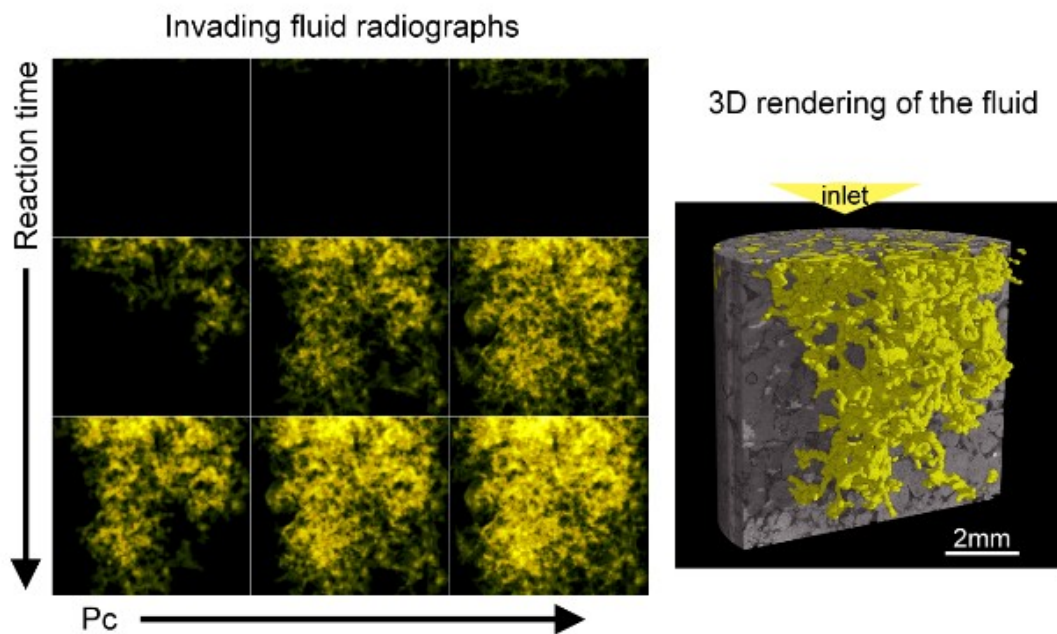


Fig. 5

805 Calculated radiographs of the invading fluid in the sample for 9 samples at different reaction time and capillary pressure. An example of the 3D calculated volume rendering (in yellow the calculated invading fluid, and in grays the measured and vertically cut volume rendering of the solid phase, are shown) of the sample in its context is shown on the right.



810

Fig. 6

Drainage curves calculated for the sample at each reaction time. Three volumes, out of the 970 calculated, are shown on the right (the calculated invading fluid in yellow, the measured solids in grays).

815

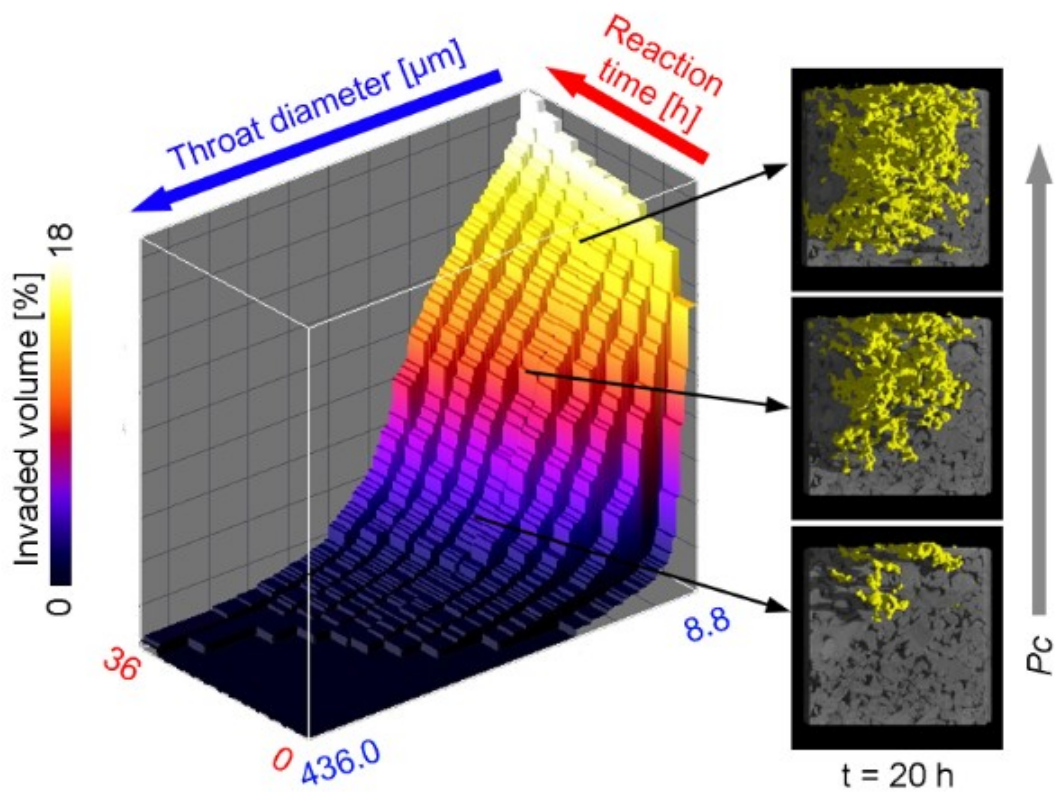
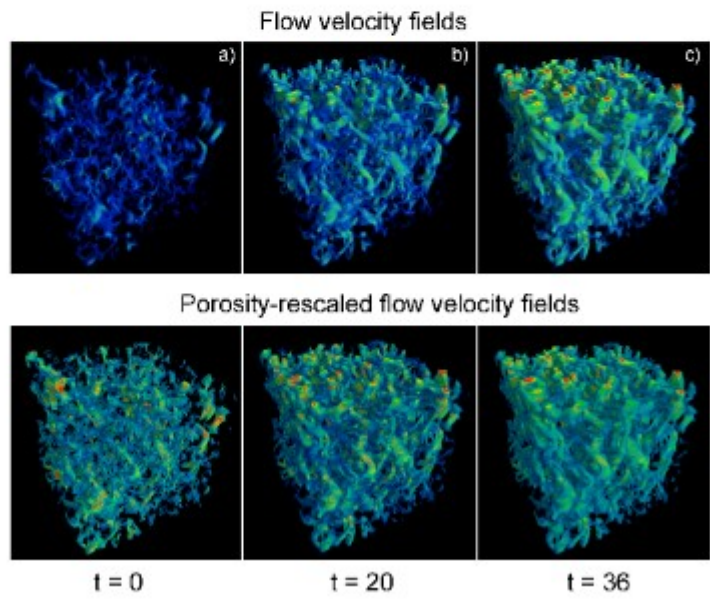
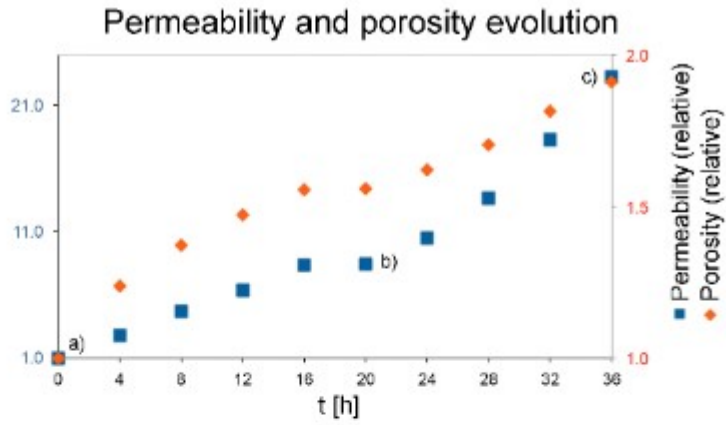


Fig. 7

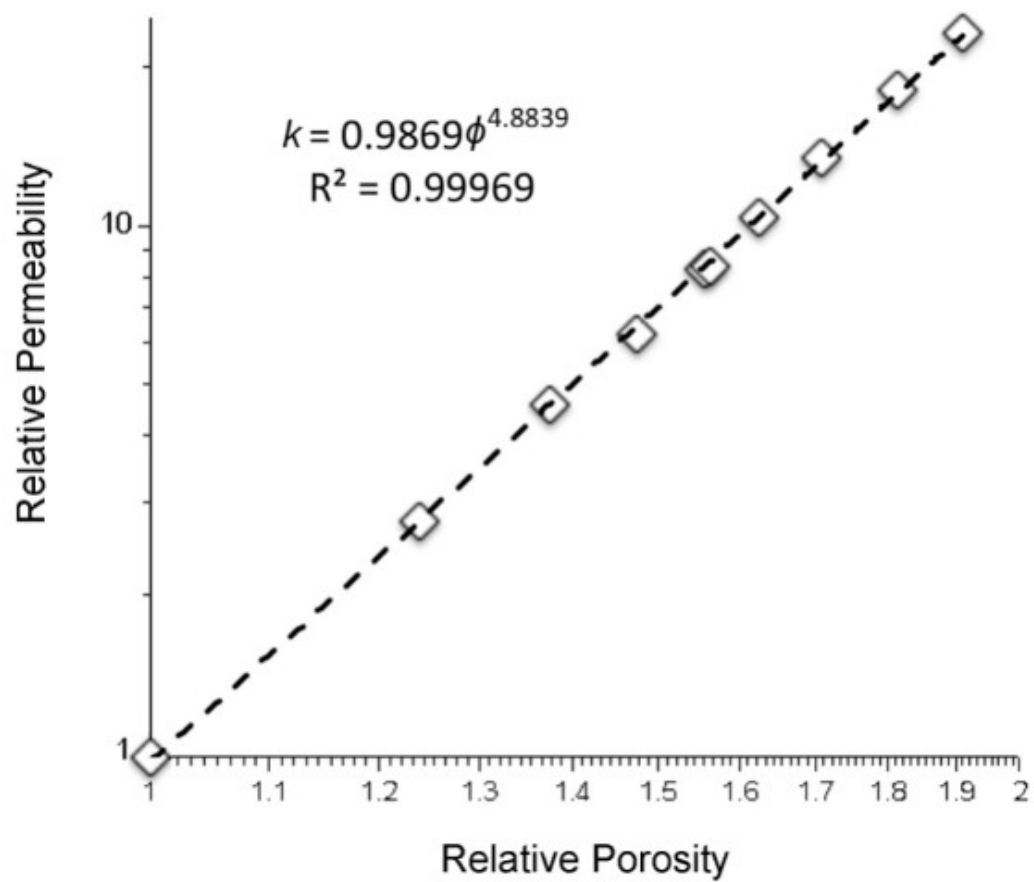
820 Top: Evolution plots for the porosity and permeability of the sample during the dissolution. Bottom: three volume renderings of the vertical flow velocity fields for the sample at three different reaction times, as calculated from the Stokes solver, and porosity-corrected to match the experimental setup conditions.



825

Fig. 8 Porosity vs. permeability diagram for the evolving sample, with power law function fit.





830

## Tables

835

t [h]	Normalized permeability	Normalized porosity	Absolute permeability [Darcy]	Absolute porosity [%]
0	1.00	1.00	1.97	11.0
4	2.79	1.24	5.49	13.6
8	4.67	1.37	9.19	15.1
12	6.35	1.47	12.49	16.2
16	8.37	1.55	16.46	17.1
20	8.45	1.56	16.62	17.2
24	10.50	1.62	20.65	17.8
28	13.66	1.70	26.87	18.8
32	18.31	1.81	36.02	19.9
36	23.30	1.91	45.83	21.0

Table 1.

Summary of the variations of porosity and permeability (as relative values: baseline = 1) and the porosity measured from the tomographic data (% of the total volume) for the sample at different stages of reaction. The permeability has been calculated via Stokes flow solver.

840